Publ. Astron. Soc. Japan (2020) 72 (4), 51 (1–13)
doi: 10.1093/pasj/psaa044
Advance Access Publication Date: 2020 May 29

VEDA: VERA data analysis software for VLBI phase-referencing astrometry

Takumi NAGAYAMA,[1,*] Tomoya HIROTA,[2,3] Mareki HONMA,[1,3] Tomoharu KURAYAMA,[4] Yuuki ADACHI,[1] Yoshiaki TAMURA,[1,3] and Yukitoshi KANYA[5]

[1]Mizusawa VLBI Observatory, National Astronomical Observatory of Japan, 2-12 Hoshigaoka-cho, Mizusawa, Oshu, Iwate 023-0861, Japan
[2]Mizusawa VLBI Observatory, National Astronomical Observatory of Japan, 2-21-1 Osawa, Mitaka, Tokyo 181-8588, Japan
[3]Department of Astronomical Sciences, SOKENDAI (The Graduate University for Advanced Studies), Osawa 2-21-1, Mitaka, Tokyo 181-8588, Japan
[4]Teikyo University of Science, 2-2-1 Senju-Sakuragi, Adachi-ku, Tokyo 120-0045, Japan
[5]Ogasawara Leonid Ltd., Asahiyama, Chichi-jima, Ogasawara, Tokyo 100-2101, Japan

*E-mail: takumi.nagayama@nao.ac.jp

Received 2020 January 20; Accepted 2020 April 16

Abstract

We present the VEra Data Analyzer (VEDA) software package for Very Long Baseline Interferometry (VLBI) phase-referencing observations and parallax measurements. The Japanese VLBI project VLBI Exploration of Radio Astrometry (VERA) provides high-precision astrometric results at the 10 μas level. To achieve this precision, accurate calibration of the atmospheric phase fluctuation, the instrumental phase, and the source structural effect is required. VEDA specializes in phase-referencing data analysis, including these calibrations. In order to demonstrate its performance we analyzed H_2O maser observations of W3(OH) and Orion KL with VERA. Their parallaxes were obtained to be 0.527 ± 0.016 mas and 2.459 ± 0.029 mas, respectively. We also analyzed their data using AIPS, which is widely used for VLBI data analysis, and confirmed that the parallaxes obtained using VEDA and AIPS are coincident within 10 μas. VEDA is available for high-precision parallax and proper motion measurements of Galactic maser sources.

Key words: astrometry — methods: data analysis — parallaxes

1 Introduction

The VLBI Exploration of Radio Astrometry (VERA) project measures the parallax and the proper motion of Galactic maser sources to reveal the three-dimensional structure of the Milky Way (Honma et al. 2000). Regular observations with VERA were started in 2004. In the 18 years until 2022, approximately 300 maser sources will be observed. The first VERA catalog that lists the parallaxes and the proper motions of maser sources will be published in the VERA PASJ special issue in 2020 (VERA Collaboration et al. 2020).

The systematic data analysis of numerous maser sources was required to create the VERA catalog. VERA aims for high parallax precision of 10 μas using the phase-referencing technique (Kobayashi et al. 2003). In order to archive this precision, accurate delay calibration for the

atmosphere, the station position, and the dual-beam instrumental delay are used (Nagayama et al. 2020). Since these calibration models and data are updated in parallel with the progress of the VERA project, data analysis based on the latest model and data is required for the best precision. Therefore, the post-processing data analysis software is a key tool for the VERA project.

In order to process the phase-referencing data analysis precisely for numerous VERA data sets, the VEra Data Analyzer (VEDA) software package has been developed by the Mizusawa VLBI Observatory in the National Astronomical Observatory of Japan (NAOJ). Astrometric results using VEDA have been published regularly (Honma et al. 2007, 2011; Niinuma et al. 2011; Chibueze et al. 2014; Yamauchi et al. 2016; Omodaka et al. 2020). We review data analysis using VEDA, and present its performance in 10 μas-level VLBI astrometry.

2 VEDA

VEDA is a software package used to perform VLBI phase-referencing data analysis and obtain parallax measurements. Figure 1 shows the data analysis flow chart for VERA. In VERA phase-referencing observations, the phase of the target maser source is calibrated using a position reference radio continuum source. In order to perform the data analysis for these two sources, 14 tasks, such as fringe search, self-calibration for the reference continuum source, Doppler tracking correction, and mapping for the target maser source are prepared in VEDA. Other data analysis software, the Astronomical Image Processing System (AIPS; Greisen 2003) has also been widely used for VERA since the first results (e.g., Hirota et al. 2007; Kim et al. 2008; Nakagawa et al. 2008). As shown in figure 1, VEDA and AIPS work in a similar way. Nevertheless, since VEDA is optimized for VERA, it is possible to get the final astrometric results with simpler operation.

VEDA is written in FORTRAN, C, and C++. Two libraries, Numerical Recipes for classical numerical analysis and PGPLOT for making scientific graphs, are used. VEDA currently runs on Red Hat Enterprise Linux 7 on the Multi-wavelength Data Analysis System (MDAS)[1] of the NAOJ Astronomy Data Center (ADC). Since there are 32 servers in MDAS, we can perform the data analysis for multiple epochs in parallel. VEDA runs with the following command line:

```
[task name] -param [parameter file name]
VERA_*** -param VERA_***.prm
```

The task names and their functions are summarized in figure 1. The parameter file is a text file to provide flexible

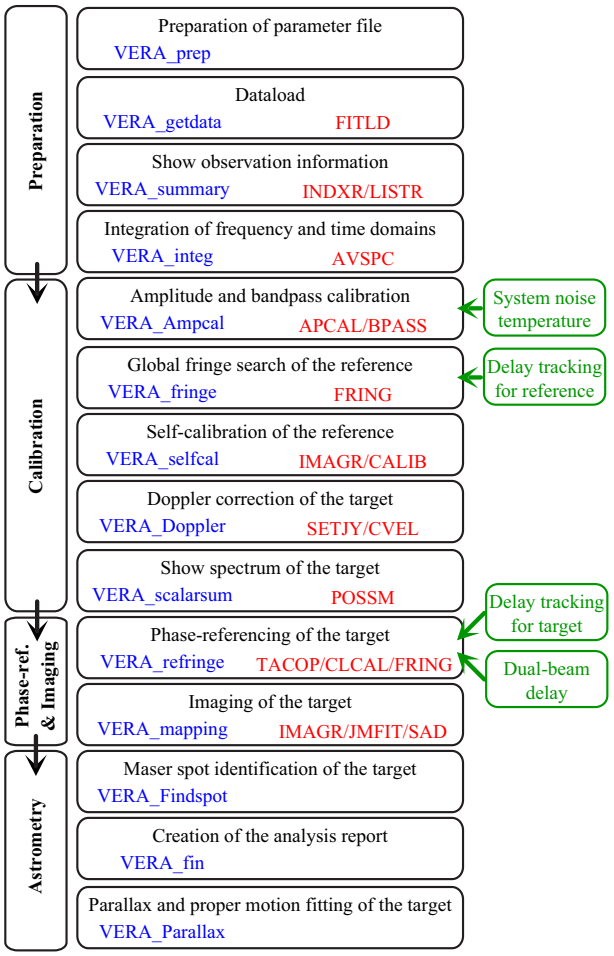

Fig. 1. Analysis flow of VEDA and AIPS. The VEDA and AIPS tasks are shown in blue and red, respectively. The calibration data used in each task is shown in green. (Color online)

specification of parameters to tasks for users. A pipeline to run tasks continuously and automatically is implemented. Using the pipeline, we can obtain the final results of the astrometic positions used for parallax measurements with only three commands.

2.1 Data structure

VEDA is available for the CODA file system, as shown in figure 2, which stores the correlation data of visibility and (u, v), and the calibration data of system noise temperature, dual-beam delay, and delay tracking. The correlation process for VERA observations was conducted by the Mitaka FX hardware correlator (Shibata et al. 1998) before 2014 and has benn conducted by the Mizusawa FX software correlator (Oyama et al. 2016) since 2015. The correlated visibility data and (u, v) data are output to the CODA file system. The system noise temperature including atmospheric attenuation is measured with the chopper-wheel method (Ulich & Haas 1976) and monitored during the

[1] ⟨https://www.adc.nao.ac.jp/MDAS/mdas_e.html⟩.

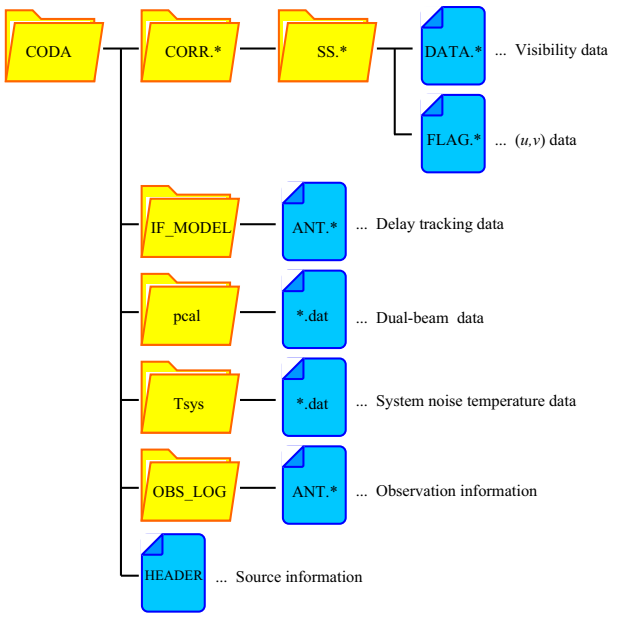

Fig. 2. CODA file system. The directory and the file are shown by yellow and blue, respectively. The correlation data of the visibility and (u, v), the calibration data of the delay tracking, the dual-beam delay, and the system noise temperature, and the information of the observation and the source are stored in each directory and file. (Color online)

observations. The instrumental delay difference between the dual beams is calibrated by the horn-on-dish method, in which artificial noise sources are mounted on the antenna feedome base and wide-band radio noise is injected into the dual-beam receivers after reflection by a subreflector (Honma et al. 2008a). The delay tracking is summarized in Nagayama et al. (2020). Since the correlator's a priori delay tracking model is not accurate enough for high-precision astrometry, recalculation of the precise delay is performed after the correlation, and the correlated visibilities are corrected for any difference between the first (rather crude) a priori tracking model and the second (more accurate) delay tracking model. The ionospheric and tropospheric delays, which are key to increasing the accuracy of the phase-referencing observations, are also calculated in this delay tracking recalculation process. The ionospheric delay is corrected based on the global ionosphere map (GIM), which is produced daily by the University of Bern. The tropospheric delay is calibrated using the troposheric zenith delay measured by GPS (Honma et al. 2008b). The Earth orientation parameter, EOP 08 C04 (IAU1980)[2] produced by the International Earth Rotation and Reference System Service is used for the calculation of the geometric delay.

[2] (Bizouard, C., & Gambis, D., 2011, The combined solution C04 for Earth Orientation Parameters consistent with International Terrestrial Reference Frame 2008, https://hpiers.obspm.fr/iers/eop/eopc04_08/C04.guide.pdf).

For AIPS, the visibility and (u, v) data are converted from CODA to FITS. The calibration data of the system noise temperature is converted to an AIPS ANTAB table. The calibration data of the delay tracking and the dual-beam instrumental delay are converted to AIPS SN tables.

3 Example of use

3.1 Data

In order to show how VEDA runs, we present a typical example of VEDA's analysis according to the flow chart in figure 1. We took the multi-epoch H_2O maser observations of W 3(OH) and Orion KL conducted from 2015 to 2018 with VERA. Since the parallaxes of W 3(OH) (Xu et al. 2006; Hachisuka et al. 2006; Matsumoto et al. 2011) and Orion KL (Hirota et al. 2007; Menten et al. 2007; Sandstrom et al. 2007; Kim et al. 2008) were accurately determined by previous VLBI observations, these two sources are good targets to verify the performance of VEDA. The observing epochs denoted by year/(day of the year) are 2015/358, 2016/250, 2016/258, 2016/259, 2017/031, 2017/059, 2017/094, 2017/122, 2017/148, 2017/267 for W 3(OH), and 2017/072, 2017/104, 2017/153, 2017/268, 2017/296, 2017/324, 2017/359, 2018/030, 2018/057 for Orion KL. The four VERA stations of Mizusawa (hereafter MZ), Iriki (IR), Ogasawara (OG), and Ishigaki-jima (IS) were used for the observations. In the two epochs 2017/268 and 2017/296 IS was not used because of problems at the antenna. The position reference sources of W 3(OH) and Orion KL are J0244+6228 (J0244+62) and J0541−0541 (J0541−05), respectively. The target and the reference sources were simultaneously observed in the dual-beam system of VERA. The delay tracking centers of these sources are summarized in table 1. The bright fringe finder 3C 84 was observed every 1–2 hr for both observations of W 3OH and Orion KL to find the fringe in the correlation processing.

The data were recorded onto the hard disk recorders OCTADISK, at a rate of 1 Gbps, and VSREC, at 4 Gbps (Oyama et al. 2016). The correlation was processed with the Mizusawa FX software correlator. The accumulation period was set to 1 s. The bandwidths and spectral channels were 16 MHz / 512 channels for W 3(OH) and 16 MHz /1024 channels for Orion KL. The corresponding frequency (velocity) spacings were 31.25 kHz (0.42 km s^{-1}) and 15.625 kHz (0.21 km s^{-1}). The bandwidths and the frequency spaces of the reference continuum sources were 512 MHz and 1 MHz for the six epochs of Orion KL from 2017/268 to 2018/057, and 240 MHz and 0.25 MHz for the other epochs.

Table 1. Source list.*

Source name	Source type	RA (J2000.0)	Dec (J2000.0)	π (mas)	$\overline{\mu}_\alpha \cos\delta$ (mas yr^{-1})	$\overline{\mu}_\delta$ (mas yr^{-1})	$\overline{v}_{\rm LSR}$ (km s^{-1})
W 3(OH)	Target	$02^{\rm h}27^{\rm m}04\overset{\rm s}{.}8393$	$+61°52'24\overset{''}{.}609$	0.527 ± 0.016	0.52 ± 0.29	-1.22 ± 0.15	-55.4 ± 1.2
J0244+6228	Reference	$02^{\rm h}44^{\rm m}57\overset{\rm s}{.}696681$	$+62°28'06\overset{''}{.}51550$				
Orion KL	Target	$05^{\rm h}35^{\rm m}14\overset{\rm s}{.}1278$	$-05°22'36\overset{''}{.}529$	2.459 ± 0.029	-0.62 ± 0.40	-7.88 ± 0.54	12.5 ± 0.8
J0541−0541	Reference	$05^{\rm h}41^{\rm m}38\overset{\rm s}{.}083371$	$-05°41'49\overset{''}{.}42843$				

*Column 1 lists the source name. Column 2 lists the source type. Columns 3 and 4 list the delay tracking center in RA and Dec, respectively. Column 5 lists the parallax. Columns 6 and 7 list the average proper motion of detected maser spots in RA and Dec, respectively. Column 8 lists the average local standard of rest (LSR) velocity of detected maser spots.

3.2 Preparation

The parameter files for the data reduction are prepared by `VERA_prep`. The visibility data and the calibration data are transferred over the network from the data server of the Mizusawa VLBI Observatory to ADC MDAS by `VERA_getdata`. Before the calibration process, we can see the basic observation information such as observational scan, station used, and frequency setting using the task `VERA_summary`. In this task, we can also see the calibration data such as the system noise temperature and the instrumental delay difference between the VERA dual beams. The integration of both time and frequency domains is done for the visibility data of the continuum source by `VERA_integ`. In the default setting, the time interval and frequency spacing after `VERA_integ` are 4 s and 1 MHz/channel, respectively.

3.3 Calibration

The amplitude and bandpass calibrations are done by `VERA_AmpCal`. The amplitude is calibrated using a two-bit quantization efficiency of $\eta = 0.88$, the system noise temperature, and the effective aperture area by an a priori calibration method summarized in Cho et al. (2017). The effective aperture area is calculated from the dish diameter of 20 m and the aperture efficiency of 41%–47% at the observation frequency of 22 GHz and 40%–50% at 43 GHz for each station. Because there is no significant change in the aperture efficiency as a function of the elevation, the gain curve is a constant value of unity. The bandpass is calibrated by the auto-correlation spectrum averaged over the observing scans of the fringe finder source by default.

The global fringe search (Schwab & Cotton 1983) for the reference source is done using `VERA_fringe` to calibrate the phase fluctuation variation caused by the atmosphere. First, a fringe search of the bright fringe finder source observed every 1–2 hr is done to find the clock offset and clock rate offset at each station. Then, based on these solutions, the fringe of the reference source is searched to obtain the fringe phases of the source. Figure 3 shows the results of a fringe search of the reference source J0541−05. They were obtained every 32 s with the averaging time for a single solution of 128 s in the default setting. The reference station was set to IR station, which is located near the center of the VERA array. The clock delay and the rate parameters in the correlation processing had already been adjusted to become the residual delay and rate within 10 ns and 20 mHz, respectively. Therefore, the residual offsets in delay and rate seen in this task are typically within these values. The baseline-based signal-to-noise ratio (SNR) is theoretically estimated to be SNR $= S_\nu/\sigma_{\rm bl} \approx$ 10–20 from the the flux density of J0541−05 of $S_\nu \approx$ 300 mJy and the thermal noise level for each baseline of $\sigma_{\rm bl} = 2k/\eta \cdot \sqrt{(T_{\rm sys1}T_{\rm sys2})}/\sqrt{(A_{\rm e1}A_{\rm e2})}/\sqrt{(2BT)} \approx$ 15–30 mJy. Here, k is the Boltzmann constant, $\eta = 0.88$ is the quantization efficiency, $T_{\rm sys1} \approx T_{\rm sys2} \approx$ 150–300 K is the system noise temperatures, $A_{\rm e1} \approx A_{\rm e2} \approx 126\,{\rm m}^2$ is the antenna effective aperture area calculated from the dish radius of 10 m and the aperture efficiency of ∼0.4, $B = 240$ MHz is the bandwidth, and $T = 128$ s is the averaging time. The SNR of each station in figure 3 typically shows 30–60. This SNR represents the sum of the baseline-based SNRs of related baselines (e.g., in the case of MZ station they are three baselines of MZ–IR, MZ–OG, and MZ–IS). Therefore, the baseline-based SNR obtained by `VERA_fringe` is typically 10–20. This value is consistent with the theoretically estimated one. The delay error caused by the thermal noise is theoretically estimated using equation (27) of Blackburn et al. (2019) to be $\sigma_\tau = \sqrt{12}/(2\pi B \cdot {\rm SNR}) \approx$ 0.1–0.2 ns. The delay dispersion seen in figure 3 is consistent with this value.

The self-calibration of the reference source by `VERA_selfcal` is done to calibrate the phase variation caused by the structure of the reference source. In the self-calibration process, the phase is solved in the first run, and the amplitude and the phase are solved in the second. CLEAN (Clark 1980), with the Cotton–Schwab algorithm (Schwab 1984), is used for the CLEAN process. For the (u, v) weight in the imaging process, UNIFORM is used as the default setting, but alternatively NATURAL can also

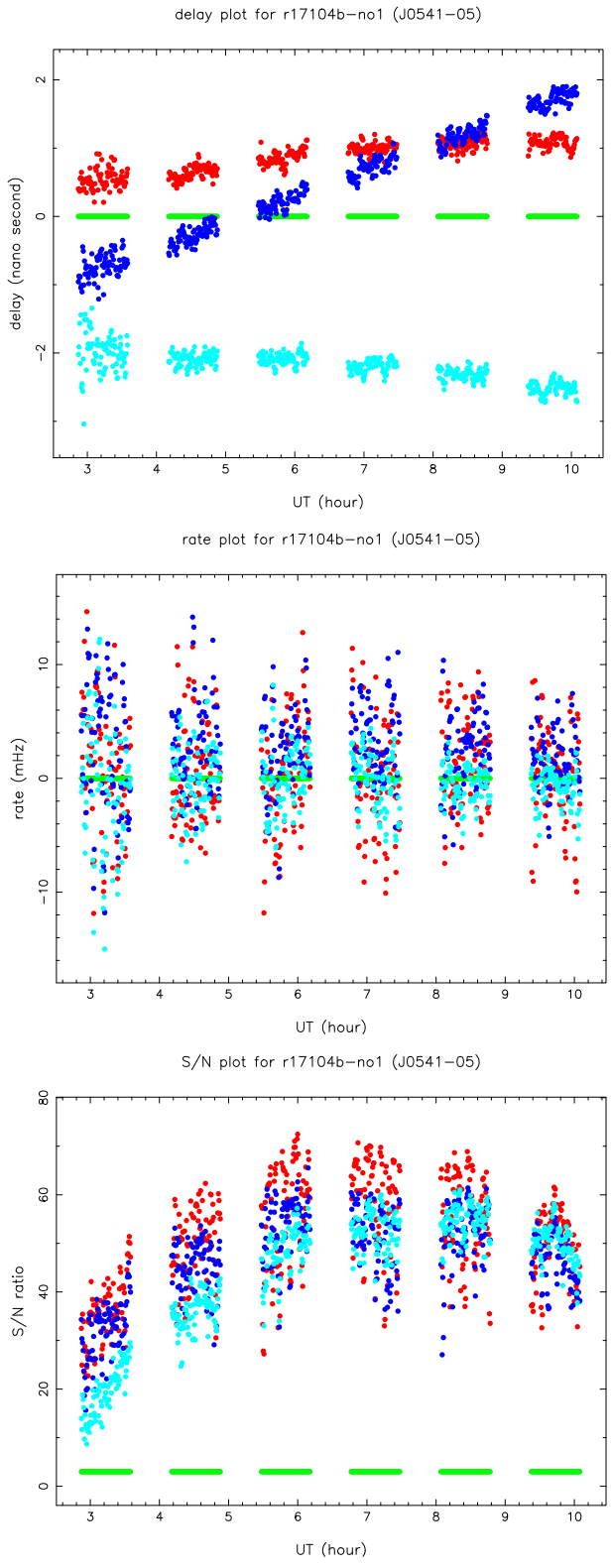

Fig. 3. Fringe search results for the reference J0541−05 obtained by `VERA_fringe`. The different color codes correspond to four antennas of VERA: MZ (red), IR (green), OG (blue), and IS (cyan). IR is the reference antenna and thus its value is identical to unity at any time. (Color online)

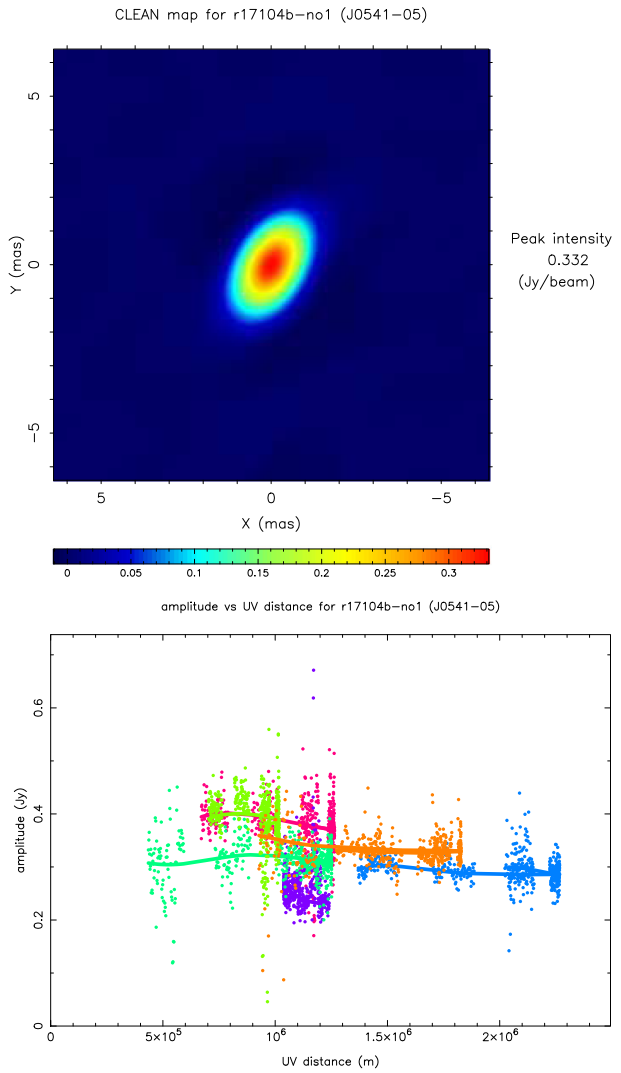

Fig. 4. Self-calibration results of the reference J0541−05 obtained by `VERA_selfcal`. (Top) Self-calibration map. In the self-calibration process, both the amplitude and phases are calibrated. (Bottom) UV distance plot. The different color codes correspond to the six baselines of VERA. The dots are the calibrated data, and the curves are the model calculated from the CLEAN components. (Color online)

be selected. We can confirm the self-calibration process and the structural effect from the CLEAN map and UV distance plot shown in figure 4, and the amplitude and phase variation in figure 5. The model of the CLEAN component shown by the solid lines in figure 4 (bottom) and figure 5 trace well the observed visibility amplitude and phase. Since the reference J0541−05 was nearly point-like, as seen in the CLEAN map, there was no strong dependence of the amplitude on the UV distance and the observed visibility phases were concentrated around 0° with a dispersion of several degrees. This dispersion is consistent with the phase error caused by the thermal noise, which is estimated to be $\sigma_\phi = 1/\mathrm{SNR} \approx 3°$–$6°$ from the baseline-based SNR of approximately 10–20.

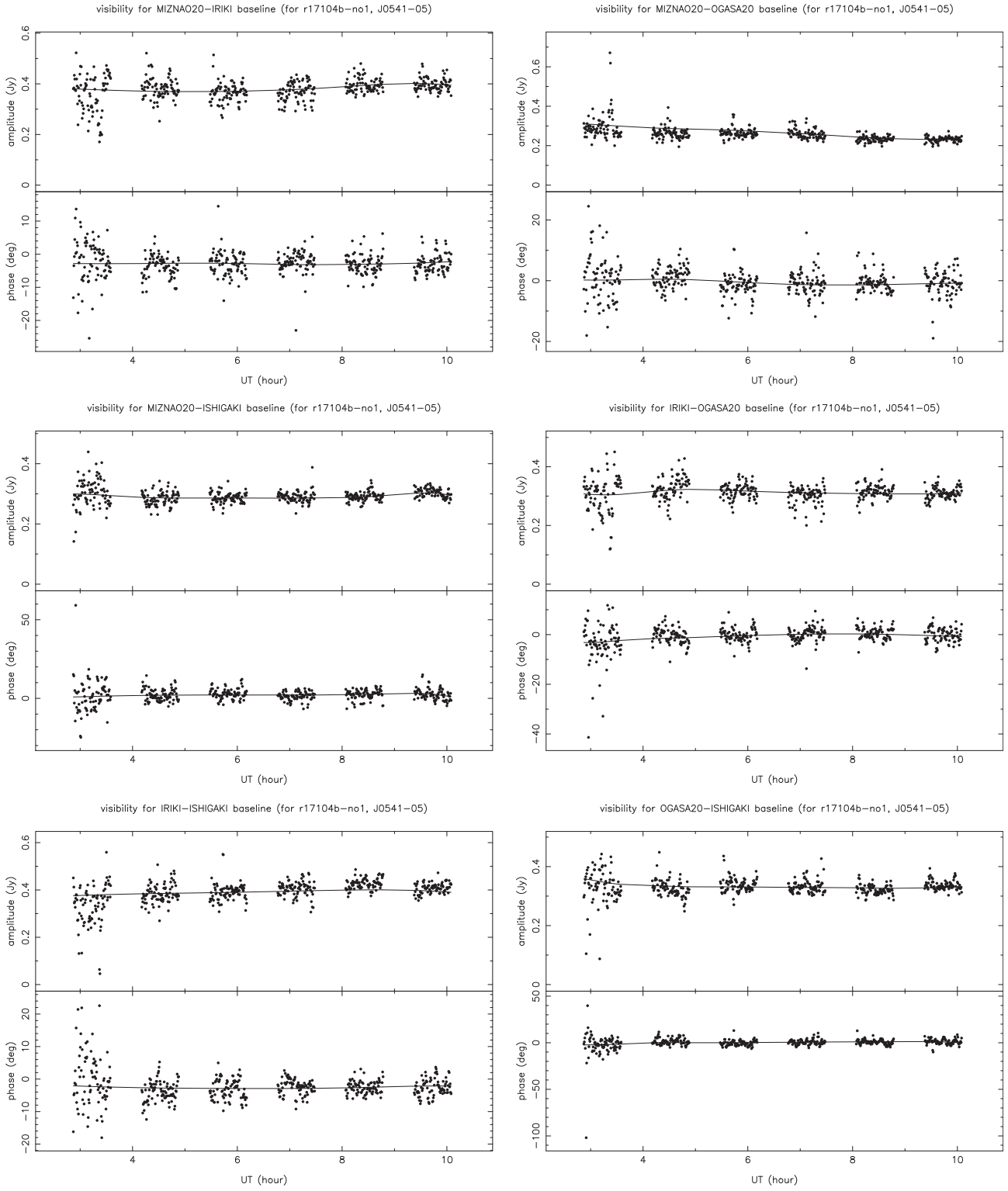

Fig. 5. Model (curve) and observed (dot) visibilities of J0541−05 for the six baselines of VERA obtained by `VERA_selfcal`. The model visibilities are obtained from the CLEAN components of the self-calibration map. The observed visibilities are corrected for the station-based gain solutions obtained with the self-calibration. The upper panel shows the visibility amplitudes, and the lower panel shows the phases.

Doppler tracking correction of the target maser source is done by `VERA_Doppler`. Its tracking frequency is calculated by $\nu_{\rm track} = \sqrt{(c - v_{\rm rad})}/\sqrt{(c + v_{\rm rad})} \cdot \nu_0$, where $v_{\rm rad} = v + v_{\rm sun} + v_{\rm mon} + v_{\rm obs}$. These velocities are projected onto the line of sight to the target source; v is the barycenter's motion with respect to Sun, $v_{\rm sun}$ is the Solar motion with respect to the LSR (Kerr & Lynden-Bell 1986), $v_{\rm mon}$ is the Earth center's motion with respect to the barycenter, $v_{\rm obs}$ is the observer's motion with respect to the Earth center, and ν_0 is the rest frequency. The auto- and cross-correlation spectra of the target maser source can be obtained by `VERA_scalarsum`, although we omit it in this paper.

3.4 Phase-referencing and imaging

The phase-referencing process of the target source is done using `VERA_refringe`. The station-based delay, rate, and phase solutions obtained by the reference continuum source are transferred and the calibration data of the dual-beam delay and phase differences are applied to the target maser visibility. When transferring the phase, the frequency difference between the target maser at each velocity channel and the reference is considered. Since this is the key process in phase-referencing, we verify it in detail by comparing with AIPS in subsection 4.1.

After the phase-referencing process, the visibility of the target maser is Fourier transformed to the dirty image and CLEANed by `VERA_mapping`. In the typical case, the intensity peak is searched from the initial dirty image with a size of $4'' \times 4''$ and a fast Fourier transform (FFT) grid of 1024. For each peak, a CLEAN image with a size of 10 mas × 10 mas and an FFT grid of 256 is created. These values can be set in the parameter file. Figure 6 shows an example of a CLEAN image of the Orion KL H_2O maser spot detected at $v_{\rm LSR} = 6.9\,{\rm km\,s^{-1}}$. The position, the peak intensity, and the image dynamic range of the maser spot are obtained from the CLEAN image. These processes of peak search, imaging, and position measurement are carried out automatically and repeatedly at the setting velocity channel range. The image center is the delay tracking center. For the exact parallax measurements, the delay tracking center was set to become the position offset of the maser spot on the phase-referencing image within 10 mas. In this case, the propagating astrometric position error is expected to be $\sim$1 μas at the source pair's separation angle of 1° (Reid & Honma 2014). The delay tracking centers of W 3(OH) and Orion KL used for the parallax measurements are summarized in table 1.

3.5 Astrometry

Realistic maser spots are identified by `VERA_Findspot`. The maser spots are regarded to be real if they are positionally

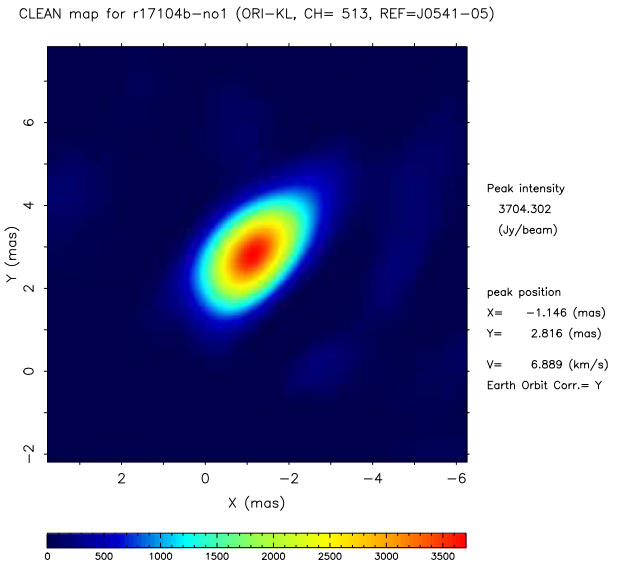

Fig. 6. Phase-referencing map of the target, Orion KL, obtained by `VERA_mapping`. The maser spot at $v_{\rm LSR} = 6.9\,{\rm km\,s^{-1}}$ is shown. The color bar shows the intensity in units of Jy beam^{-1}. The values of peak intensity and position are shown on the right side of the figure. (Color online)

coincident within 1 mas (corresponding to 1 au at a source distance of 1 kpc) over at least two consecutive velocity channels. Since an H_2O maser feature, which is a cluster of maser spots and represents a physical feature, has a typical size of $\sim$1 au and a typical Doppler velocity dispersion of $\sim$0.5 km s^{-1} (Gwinn 1994), maser spots are mostly detected at similar positions and in consecutive velocity channels. The identification criteria of `VERA_Findspot` are based on this physical maser feature.

Documentation of the data analysis is created by `VERA_fin` to summarize the plots and maps, as shown in figures 3 to 6. The processes from `VERA_prep` to `VERA_fin` are the data analysis of a single epoch, and they can be run continuously by `VERA_Pipeline`. Although the processing time depends on the data size, in particular the imaging size and the channel number, it is typically 4 hr epoch^{-1} using a single core of MDAS. The data analysis of a single epoch is run fully automatically by `VERA_Pipeline`, while the processes of combining the results of multiple epochs and obtaining the parallax (mentioned in the next paragraph) are still done manually by the analyst.

The fitting of the parallax and proper motion is done by `VERA_Parallax`. The positional variation of the target maser spot obtained by the multi-epoch analysis is fitted with a parallax of π, a proper motion in the right ascension and declination directions of $(\mu_\alpha \cos\delta, \mu_\delta)$, and a position offset origin of $(\Delta\alpha_0 \cos\delta, \Delta\delta_0)$ by the least squares method. Figure 7 shows the examples of W 3(OH) and Orion KL, whose maser spots are at $v_{\rm LSR} = -48.3\,{\rm km\,s^{-1}}$ and $6.9\,{\rm km\,s^{-1}}$, respectively. The spiral motion which is the

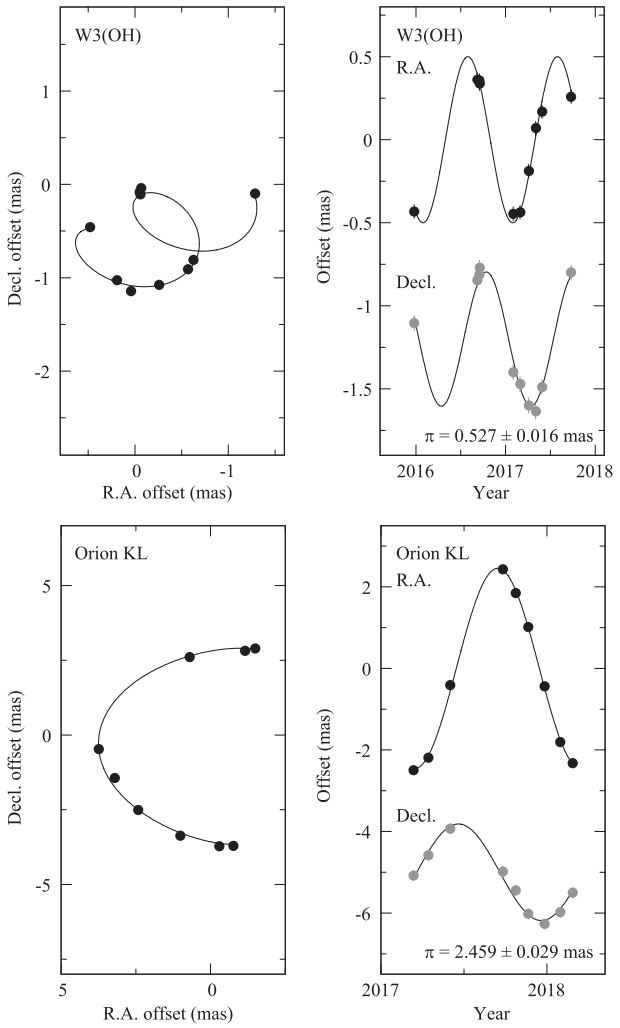

Fig. 7. Parallax and proper motion data and fits of W 3(OH) (top) and Orion KL (bottom). The positional variation on the sky is shown in the left panel, and the parallax after removing the proper motion is shown in the right panel. The solid lines indicate the parallax and proper motion fit curves.

sum of the parallax motion and the proper motion can be seen on the sky in figure 7 (left). As can be seen in figure 7 (right), the positional variation after removing the proper motion shows the sinusoidal motion with a period of 1 yr caused by the parallax. The amplitude corresponds to the parallax. The parallaxes of W 3(OH) and Orion KL were obtained by the fitting to be $\pi = 0.527 \pm 0.016$ mas (corresponding to a source distance of $D = 1.90 \pm 0.06$ kpc) and $\pi = 2.459 \pm 0.029$ mas ($D = 407 \pm 5$ pc), respectively. The other parameters obtained, as well as the parallax, are summarized in table 2. For W 3(OH) and Orion KL, the standard deviations of the post-fit residuals were $(\sigma_\alpha, \sigma_\delta)_{\rm res} = (0.040, 0.045)$ mas and (0.060, 0.123) mas, respectively. The position errors caused by the thermal noise calculated by $\sigma_{\rm the} \approx 0.5 \cdot \theta_{\rm beam}/{\rm SNR}$ were $\sigma_{\rm the} \approx 0.002$–$0.027$ mas and 0.003–0.017 mas, respectively. Here, $\theta_{\rm beam}$ is the synthesized beam size and SNR is the dynamic range of the maser spot on the phase-referencing image. The error floors which were added in quadrature to $\sigma_{\rm the}$ to achieve the reduced χ^2 value of unity (Reid et al. 2009) were $(\sigma_\alpha, \sigma_\delta)_{\rm flr} = (0.037, 0.041)$ mas and (0.059, 0.122) mas, respectively. These error floors mainly originate from the systematic position errors from uncalibrated tropospheric delay and the source structural effect (Nagayama et al. 2015, 2020).

4 Verification

4.1 Phase-referencing

The same visibility and calibration data set of W 3(OH) and Orion KL were reduced via VEDA and AIPS, and their results compared. Figure 8 shows the phase-referenced phase of the target source obtained by VEDA `VERA_refringe` and AIPS FRING. The solutions were obtained with a solution averaging time of 64 s and time interval of 16 s. This is the phase which was applied to the solutions of the fringe fitting and the self-calibration of the reference source and the calibration data of the dual-beam instrumental phase difference and the delay tracking. Therefore, this presents the phase variation caused by the position offset of the target maser spot, the structural effect of the spot (if there is any structure), and phase errors that are not corrected properly. The position offsets (with respect to the tracking center position used in

Table 2. Parallax and proper motion fits.*

Source name	Software	π (mas)	$\mu_\alpha \cos\delta$ (mas yr^{-1})	μ_δ (mas yr^{-1})	$\Delta\alpha_0 \cos\delta$ (mas)	$\Delta\delta_0$ (mas)	σ_α (mas)	σ_δ (mas)
W 3(OH)	VEDA	0.527 ± 0.016	0.62 ± 0.03	-0.38 ± 0.03	-0.86 ± 0.03	-0.19 ± 0.04	0.040	0.045
	AIPS	0.534 ± 0.017	0.57 ± 0.03	-0.36 ± 0.04	-0.80 ± 0.04	-0.22 ± 0.04	0.054	0.031
Orion KL	VEDA	2.459 ± 0.029	0.59 ± 0.06	-6.45 ± 0.13	0.99 ± 0.04	2.97 ± 0.08	0.060	0.123
	AIPS	2.461 ± 0.033	0.56 ± 0.07	-6.40 ± 0.11	1.02 ± 0.05	2.93 ± 0.07	0.068	0.099

*Column 1 lists the source name. Column 2 lists the analysis software. Column 3 lists the parallax. Columns 4 and 5 list the proper motion in RA and Dec, respectively. Columns 6 and 7 list the position offset origin in RA and Dec, respectively, with respect to the coordinate in table 1. Columns 8 and 9 list the post-fit residual rms in RA and Dec, respectively.

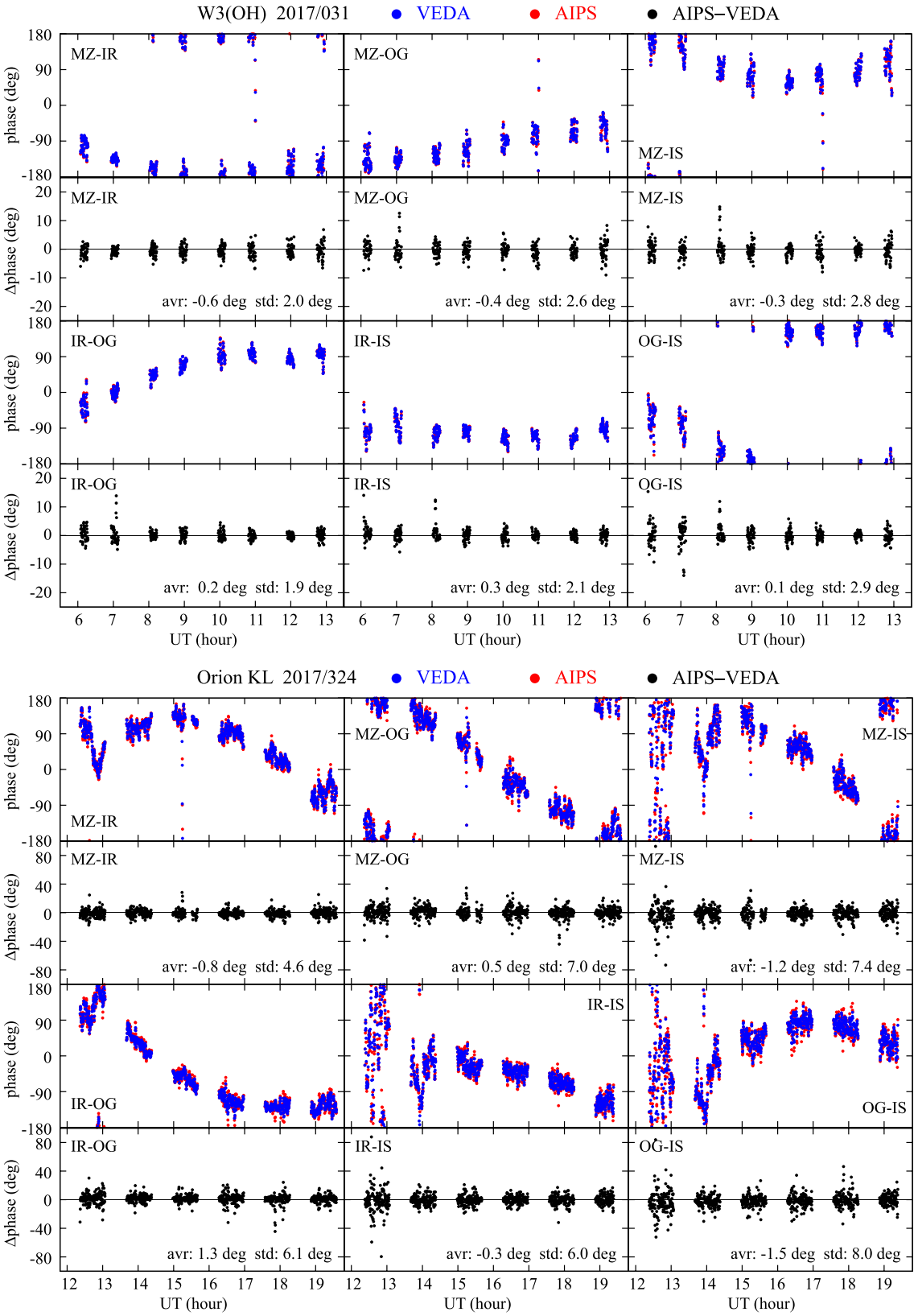

Fig. 8. Residual phases of W3(OH) (top) and Orion KL (bottom). The phases obtained by VEDA (blue) and AIPS (red), and their difference AIPS − VEDA (black) are shown. Here, residual phases include the position offsets and the structural effect of the maser spots as well as the calibration residuals (see text). The average and the standard deviation of AIPS − VEDA are shown in the bottom right corner of each panel. (Color online)

the delay tracking) of W 3(OH) and Orion KL obtained by the phase-referencing maps are $(\Delta\alpha\cos\delta,\ \Delta\delta) = (-0.623,\ -0.811)$ mas and (2.414, −2.506) mas, respectively. Therefore, the sinusoidal phase variation with a 24 hr period corresponding to these position offsets can be seen. The phase variations obtained by VEDA and AIPS were consistent. The difference AIPS − VEDA was concentrated around 0° and a significant systematic offset could not be found in any of the six baselines. The average offset of the difference was within 2°, corresponding to an astrometric position offset of $\theta_{\rm beam}\cdot(2^\circ/360^\circ) = 0.005$–$0.01$ mas at the synthesized beam size of $\theta_{\rm beam} = 1$–2 mas. This indicates that the phase calibration performance of VEDA is equivalent to that of AIPS for phase-referencing astrometry at the 0.01 mas level.

As shown in the Orion KL data of figure 8, large phase scatter can be seen at the beginning of the observation. This is due to the low elevation of the source: toward low elevations, the system noise temperature becomes high, and in addition the effect of the tropospheric delay offset becomes significant. This phase scatter appeared when $\Delta\sec Z = |\sec Z_{\rm tar} - \sec Z_{\rm ref}| \geq 0.1$, where $Z_{\rm tar}$ and $Z_{\rm ref}$ are the zenith angles of the target and the reference sources, respectively. The corresponding positional error is estimated to be $\Delta\theta = c\tau_{\rm err}\Delta\sec Z/D \geq 0.2$ mas from a tropospheric zenith delay error of $c\tau_{\rm err} \approx 20$ mm (Honma et al. 2008b) and VERA's maximum baseline length of $D = 2300$ km. Since this phase scatter seen at $\Delta\sec Z \geq 0.1$ degrades the quality of the phase-referencing image and causes the large position error, we flagged out this data in this analysis.

4.2 Parallax measurement

We compared the parallaxes obtained by VEDA and AIPS for W 3(OH) and Orion KL. Their parallaxes were consistent at the 0.01 mas level. The parallaxes obtained by VEDA and AIPS are shown in figure 9, and the results of the parallax fitting are summarized in table 2. The post-fit residuals of $(\sigma_\alpha,\ \sigma_\delta)$ in table 2 were approximately (0.04, 0.04) mas for W 3OH and (0.06, 0.11) mas for Orion KL, and were comparable between VEDA and AIPS; this indicates that the performance for the parallax measurement of VEDA is equivalent to that of AIPS. The geometric averages of σ_α and σ_δ were 0.04 mas for W 3OH and 0.08 mas for Orion KL. These are consistent with the position error caused by a tropospheric zenith delay error of $c\tau_{\rm err} \approx 20$ mm (Honma et al. 2008b), which were estimated to be 0.04 mas for W 3OH and 0.09 mas for Orion KL by $\Delta\theta = c\tau_{\rm err}\Delta\sec Z/D$ using the baseline length of $D = 2300$ km, $\Delta\sec Z \approx 0.02$ for W 3OH, and $\Delta\sec Z \approx 0.05$ for Orion KL.

More directly, we compared the phase-referenced positions obtained by VEDA and AIPS. Their positions were consistent at the 0.03 mas level. The position difference between them (AIPS − VEDA) is shown in figure 9. The average of the difference was 0.01–0.02 mas and the standard deviation of the difference was 0.03 mas for both sources, W 3(OH) and Orion KL. The average can be ignored for the parallax measurement. The standard deviation of 0.03 mas would propagate to the parallax error of $0.03\ {\rm mas}/\sqrt{10} \approx 0.01$ mas with ten observations. This corresponds to 10% of the parallax at a distance of 10 kpc. The standard deviation of 0.03 mas is larger than the position error of the thermal noise of ∼0.01–0.02 mas (see subsection 3.5). Therefore, the systematics are significant. Since, as mentioned in previous section, the phase-referenced phases of VEDA and AIPS were consistent to within 2°, corresponding to a position offset of 0.005–0.01 mas, the position difference of 0.03 mas could originate with the latter processes of the imaging and/or the position fitting of the maser spot. The standard deviation of 0.03 mas is smaller than the post-fit residual of the parallax fitting, which is equivalent to a tropospheric zenith delay error of ∼20 mm. This is because the same tropospheric calibration correction, based on the tropospheric zenith delay measured by GPS (Honma et al. 2008b) and Niell's mapping function (Niell 1996), are used in both AIPS and VEDA analysis. Therefore, the calibration errors have common effects and cause similar position offsets in the analysis results.

The VEDA parallaxes obtained are also consistent with those of the previous parallax measurements with VLBI and Gaia for W 3(OH) (Xu et al. 2006; Hachisuka et al. 2006; Matsumoto et al. 2011; Navarete et al. 2019) and Orion KL (Hirota et al. 2007; Menten et al. 2007; Sandstrom et al. 2007; Kim et al. 2008; Kounkel et al. 2017, 2018). In addition to W 3(OH) and Orion KL, we also compared the parallaxes newly obtained by VEDA and previously obtained by AIPS for the 12 sources WB673, G200.08−01.63, G037.50+00.53, G037.82+00.41, G044.31+00.04, G061.48+00.10, ON 1, ON 2N, G080.70+00.70, V637 Per, BX Eri, and HS UMa (VERA Collaboration et al. 2020 and references therein). The correlation plot of these 14 sources is shown in figure 10. The agreement between VEDA and AIPS is excellent for all sources, with the slope of the fitted line consistent with unity and the intercept consistent with zero within 1σ. The slope and the intercept are obtained to be $a = 0.990 \pm 0.010$ and $b = 0.001 \pm 0.011$ mas, respectively. Thus, significant systematical differences were not found between VEDA and AIPS.

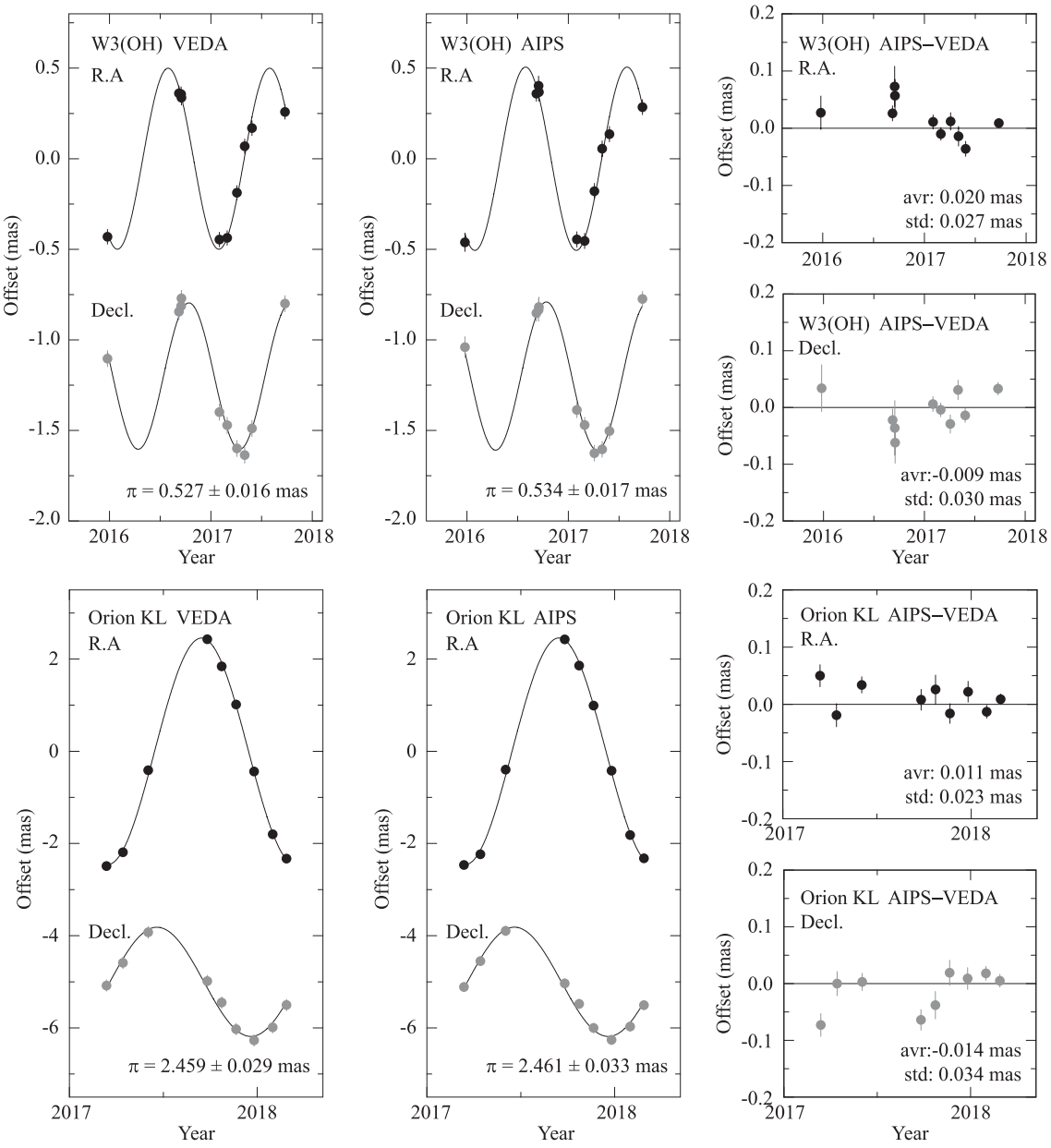

Fig. 9. Parallaxes of W3(OH) (top) and Orion KL (bottom). The parallaxes obtained by VEDA (left) and AIPS (middle), and the position differences of AIPS − VEDA (right), are shown. The black and gray dots show the RA and Dec directions, respectively. The error bar in the left and middle panels is the root-sum-square of the thermal noise position error and the error floor, $\sqrt{(\sigma_{\rm the}^2 + \sigma_{\rm flr}^2)}$. The error bar in the right panel is $\sigma_{\rm the}$.

4.3 Wide-field mapping

In the previous sections we focused on a single maser spot whose position offset with respect to the delay tracking center was within 10 mas (see subsection 3.4). On the other hand, numerous maser spots are distributed over ∼1″–10″ in the case of H_2O masers in a star-forming region. Their wide-field mapping and proper motion measurement can reveal the velocity field in the star-forming region. However, there is an issue as to how to measure the position exactly in such a wide field. The precision of the position measurement degrades with increasing position offset with respect to the delay tracking center due to the uncertainty of (u, v) and the smearing effect. In order to address this issue, we used multiple tracking centers. In this section we present examples of the wide-field mapping of H_2O maser spots using VEDA.

Figure 11 shows the H_2O maser spot map of W3(OH) and Orion KL. Their LSR velocity ranges were set to $-90 \le v_{\rm LSR} \le -30\,{\rm km\,s^{-1}}$ and $-40 \le v_{\rm LSR} \le 60\,{\rm km\,s^{-1}}$, respectively, from the cross-correlated spectra obtained by `VERA_scalarsum`. Their mapping areas were set to 4″ × 4″ and 36″ × 44″, respectively, from the fringe rate maps.

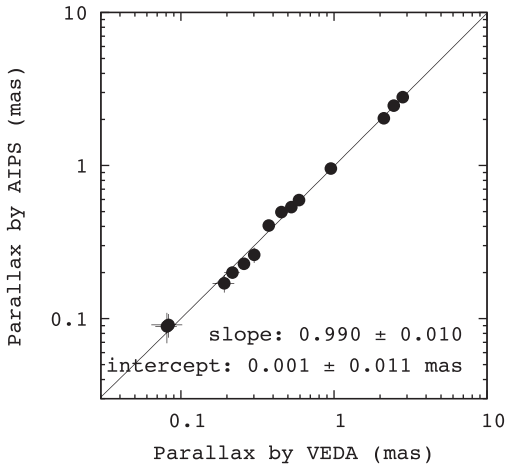

Fig. 10. Comparison of the parallaxes obtained by VEDA ($\pi_{\rm VEDA}$) and AIPS ($\pi_{\rm AIPS}$). The solid line shows the linear fit to $\pi_{\rm AIPS} = 0.990 \cdot \pi_{\rm VEDA} + 0.001$ mas.

All ten observing epochs were mapped for W 3(OH), while three representative epochs of 2017/324, 2018/030, and 2018/057 were mapped for Orion KL, because its area was too large to map all the epochs. We measured the proper motions of the maser spots detected at more than three epochs. Then, the parallaxes of W 3(OH) and Orion KL were fixed to 0.527 mas and 2.459 mas, respectively, as obtained in subsection 3.5.

In the case of Orion KL, imaging at a large position offset of approximately 20″ is required. The position is measured in the image domain. This is performed by a two-dimensional Fourier transformation from the visibility (u, v) data to the sky coordinate, i.e., $(u, v) \rightarrow (x, y)$. This provides the position offset with respect to the delay tracking center of $(\Delta x, \Delta y)$. The difference of (u, v) separated by Δx is estimated to be $\Delta u \approx u \cdot \Delta x$. If this Δu is not corrected and the original (u, v) is used directly for the imaging at the position offset of $\Delta x \approx 20'' \approx 10^{-4}$ rad, the propagating position error is estimated to be $\Delta x_{\rm err} \approx \Delta u/u \cdot \Delta x \approx 10^{-4} \cdot 20'' \approx 2$ mas. This also seriously degrades the image. In order to reduce this error and the image degradation, Δu or Δx should be corrected before the imaging. Therefore, the area of $36'' \times 44''$ was separated into a 9×11 grid $= 99$ sub-areas of $4'' \times 4''$. For each sub-area, the delay tracking center was set in the delay tracking recalculation process, and then `VERA_refringe` and `VERA_mapping` were performed. Although the uncertainty of $\Delta u/u \approx 10^{-4}$ still remains, the position offset can be reduced to $\Delta x \approx 2''$. Then, the propagating position error is estimated to be $\Delta x_{\rm err} \approx 0.2$ mas. In the case of a position error of $\Delta x_{\rm err} \approx 0.2$ mas and a time interval between observing epochs of $\Delta t \approx 0.2$ yr, the proper motion error is estimated to be $\Delta \mu \approx \Delta x/\Delta t \approx 1$ mas yr^{-1}, corresponding to approximately 10% of the typical internal motion of Orion KL. This effect is not serious for W 3(OH), so its delay tracking center was set to the center of the distribution, $(\alpha, \delta)_{\rm J2000.0} = (02^{\rm h}27^{\rm m}04\overset{\rm s}{.}6800, +61°52'24\overset{''}{.}566)$. The position error and the proper motion error of W 3(OH) are estimated to be $\Delta x_{\rm err} \approx 0.02$ mas and $\Delta \mu \approx 0.1$ mas yr^{-1}, respectively. This proper motion error corresponds to approximately 3% of the typical internal motion of W 3(OH).

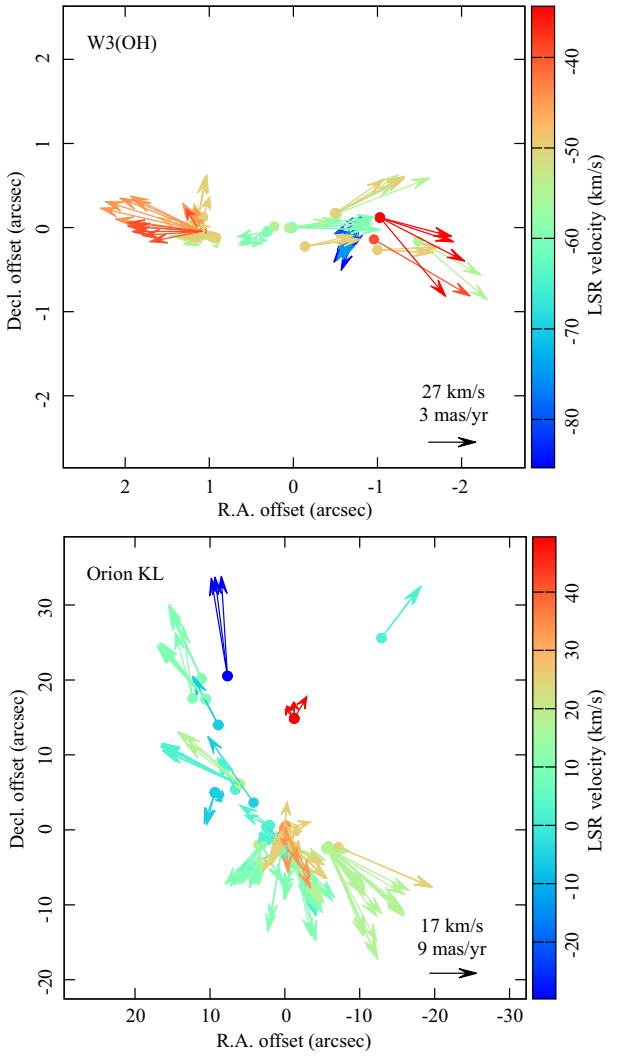

Fig. 11. Wide-field maps of H_2O masers in W 3(OH) (top) and Orion KL (bottom). The map origin is $(\alpha, \delta)_{\rm J2000.0} = (02^{\rm h}27^{\rm m}04\overset{\rm s}{.}6800, +61°52'24\overset{''}{.}566)$ for W 3(OH) and $(05^{\rm h}35^{\rm m}14\overset{\rm s}{.}1278, -05°22'36\overset{''}{.}529)$ for Orion KL, respectively. (Color online)

The proper motions of 112 maser spots for W 3(OH) and 217 maser spots for Orion KL were measured. The average proper motion and the average LSR velocity were calculated and are summarized in table 1. The error is the standard error. The arrows in figure 11 show the residual proper motion vectors, which are the differences between the proper motions of individual spots and the average,

and represent the internal motions of the maser spots. The distribution and the internal motion of W 3(OH) are consistent with previous VLBI observations (Alcolea et al. 1993; Hachisuka et al. 2006). In previous VLBI observations of Orion KL, the maser spots were associated with the central "low velocity (18 km s^{-1}) flow" and the outside "high velocity (30–100 km s^{-1}) flow" (Genzel et al. 1981). Our detected maser spots appear to be associated with the "low velocity (18 km s^{-1}) flow," while maser spots from the "high velocity (30–100 km s^{-1}) flow" were not detected in the three epochs analyzed. This could be because of the high time variation of the high velocity spot (Genzel et al. 1981). Since the overall distribution and internal motion obtained by VEDA trace well those of previous observations, VEDA is suitable for wide-field mapping at the 20″ level.

5 Summary

We have developed data analysis software specialized for VERA, VEDA, that provides reliable astrometric results for the parallax and proper motion. We demonstrated that VEDA is suitable for parallax measurement at the 10 μas level. The parallaxes of W 3(OH) and Orion KL were obtained using VEDA to be 0.527 $\pm$ 0.016 mas and 2.459 $\pm$ 0.029 mas, respectively. These are consistent with the parallaxes obtained using AIPS within 10 μas and the parallaxes of previous measurements with VERA, VLBA, and Gaia within errors. The phase-referenced phases calibrated by VEDA and AIPS are also consistent to within 2°, corresponding to an astrometric position offset of 10 μas.

We performed wide-field mapping of H_2O maser spots in W 3(OH) and Orion KL using VEDA. The errors in position and proper motion were 0.02 mas and 0.1 mas yr^{-1} at a position offset (with respect to the delay tracking center) of 2″, and 0.2 mas and 1 mas yr^{-1} at a position offset of 20″. These would correspond to approximately 10% of the internal proper motion for most H_2O maser spots in star-forming regions. For higher precision, the (u, v) offset caused by the position offset should be corrected.

Acknowledgment

We are grateful to a referee for valuable comments and suggestions which improved the manuscript. Data analysis was (in part) carried out on the Multi-wavelength Data Analysis System operated by the Astronomy Data Center (ADC), National Astronomical Observatory of Japan. TH is financially supported by MEXT/JSPS KAKENHI Grant Number 17K05398.

References

Alcolea, J., Menten, K. M., Moran, J. M., & Reid, M. J. 1993, Astrophysical Masers (Berlin: Springer), 225
Blackburn, L., et al. 2019, ApJ, 882, 23
Chibueze, J. O., et al. 2014, ApJ, 784, 114
Cho, I., et al. 2017, PASJ, 69, 87
Clark, B. G. 1980, A&A, 89, 377
Genzel, R., Reid, M. J., Moran, J. M., & Downes, D. 1981, ApJ, 244, 884
Greisen, E. W. 2003, in Information Handling in Astronomy – Historical Vistas, ed. A. Heck (Dordrecht: Kluwer Academic Publishers), 109
Gwinn, C. R. 1994, ApJ, 429, 253
Hachisuka, K., et al. 2006, ApJ, 645, 337
Hirota, T., et al. 2007, PASJ, 59, 897
Hirota, T., et al. 2008, PASJ, 60, 961
Honma, M., et al. 2007, PASJ, 59, 889
Honma, M., et al. 2008, PASJ, 60, 935
Honma, M., et al. 2010, Pub. Natl. Astron. Obs. Jpn., 13, 57
Honma, M., et al. 2012, PASJ, 64, 136
Honma, M., Hirota, T., Kan-Ya, Y., Kawaguchi, N., Kobayashi, H., Kurayama, T., & Sato, K. 2011, PASJ, 63, 17
Honma, M., Kawaguchi, N., & Sasao, T. 2000, Proc. SPIE, 4015, 624
Honma, M., Tamura, Y., & Reid, M. J. 2008, PASJ, 60, 951
Kerr, F. J., & Lynden-Bell, D. 1986, MNRAS, 221, 1023
Kim, M. K., et al. 2008, PASJ, 60, 991
Kobayashi, H., et al. 2003, in ASP Conf. Ser., 306, New Technologies in VLBI, ed. Y. C. Minh (San Francisco: ASP), 367
Kounkel, M., et al. 2017, ApJ, 834, 142
Kounkel, M., et al. 2018, AJ, 156, 84
Kuhn, M. A., Hillenbrand, L. A., Sills, A., Feigelson, E. D., & Getman, K. V. 2019, ApJ, 870, 32
Matsumoto, N., et al. 2011, PASJ, 63, 1345
Menten, K. M., Reid, M. J., Forbrich, J., & Brunthaler, A. 2007, A&A, 474, 515
Nagayama, T., et al. 2015, PASJ, 67, 65
Nagayama, T., et al. 2020, 72, 52
Nakagawa, A., et al. 2008, PASJ, 60, 1013
Navarete, F., Galli, P. A. B., & Damineli, A. 2019, MNRAS, 487, 2771
Niell, A. E. 1996, J. Geophys. Res., 101, 3227
Niinuma, K., et al. 2011, PASJ, 63, 9
Omodaka, T., et al. 2020, PASJ, 72, 55
Oyama, T., et al. 2016, PASJ, 68, 105
Reid, M. J., & Honma, M. 2014, ARA&A, 52, 339
Reid, M. J., Menten, K. M., Brunthaler, A., Zheng, X. W., Moscadelli, L., & Xu, Y. 2009, ApJ, 693, 397
Sandstrom, K. M., Peek, J. E. G., Bower, G. C., Bolatto, A. D., & Plambeck, R. L. 2007, ApJ, 667, 1161
Schwab, F. R. 1984, AJ, 89, 1076
Schwab, F. R., & Cotton, W. D. 1983, AJ, 88, 688
Shibata, K. M., Kameno, S., Inoue, M., & Kobayashi, H. 1998, in ASP Conf. Ser., 144, IAU Colloq. 164, Radio Emission from Galactic and Extragalactic Compact Sources, ed. J. A. Zensus et al. (San Francisco: ASP), 413
Ulich, B. L., & Haas, R. W. 1976, ApJS, 30, 247
VERA Collaboration et al. 2020, PASJ, 72, 50
Xu, Y., Reid, M. J., Zheng, X. W., & Menten, K. M. 2006, Science, 311, 54
Yamauchi, A., Yamashita, K., Honma, M., Sunada, K., Nakagawa, A., & Ueno, Y. 2016, PASJ, 68, 60